

# Nuclear Magnetic Resonance model of an entangled sensor under noise

Le Bin Ho,<sup>1</sup> Yuichiro Matsuzaki,<sup>2</sup> Masayuki Matsuzaki,<sup>3</sup> and Yasushi Kondo<sup>1</sup>

<sup>1</sup>*Department of Physics, Kindai University, Higashi-Osaka, 577-8502, Japan*

<sup>2</sup>*Nanoelectronics Research Institute, National Institute of Advanced Industrial Science and Technology (AIST), 1-1-1 Umezono, Tsukuba, Ibaraki 305-8568, Japan*

<sup>3</sup>*Department of Physics, Fukuoka University of Education, Munakata, Fukuoka 811-4192, Japan*

Entangled sensors have been attracting much attention recently because they can achieve higher sensitivity than those of classical sensors. To exploit entanglement as a resource, it is important to understand the effect of noise, because the entangled state is highly sensitive to noise. In this paper, we present a Nuclear Magnetic Resonance (NMR) model of an entangled sensor in a controlled environment; one can implement the entangled sensor under various noisy environments. In particular, we experimentally investigate the performance of the entangled sensor under time-inhomogeneous noisy environments, where the entangled sensor has the potential to surpass classical sensors. Our “entangled sensor” consists of a multi-spin molecule solved in isotropic liquid, and we can perform, or simulate, quantum sensing by using NMR techniques.

## I. INTRODUCTION

Quantum sensing has been attracting much attention recently as an application of quantum mechanics like quantum information technology [1], because it may achieve better sensitivity than a classical sensor. Quantum sensing may be divided into three categories according to what aspect of quantum mechanics employed to improve the performance of measurements: (i) quantum objects such as electrons or nuclear spins, (ii) quantum coherence such as superposition states or matter-wave-like nature, and (iii) quantum entanglement, which cannot be described classically [2]. The third may be the most quantum-like, and various efforts have been reported regarding this category. Among these, entanglement-enhanced magnetic field sensing with atomic vapors was reported, such as spin squeezing (entanglement) within the atomic internal structure [3], and employing entanglement between two vapor cells [4] to reduce noise. A more direct approach to enhance the sensitivity of measurements using entanglement was presented [5], and experimental efforts using trapped ions [6–9], ultra-cold atoms [10, 11], and NMR [12, 13] have been reported.

A potential problem involved in entangled sensors is their fragility to noise. In fact, it has been theoretically proven that an entangled sensor in a Markovian noisy environment, where relaxation is exponential, cannot overcome the standard quantum limit (SQL) [14]. On the other hand, there are numerous theoretical predictions indicating that an entangled sensor can outperform a classical sensor under the effect of a time-inhomogeneous noisy environment, which induces a non-exponential decay [15–18]. However, there have been no experimental demonstrations yet for the latter case. Therefore, it is very important to study the behavior of entangled sensors under the effect of time-inhomogeneous noisy environments.

In this work, we investigate the behavior of an entangled sensor in a controlled environment using NMR. Although the demonstration does not constitute a formal proof of the quantum-mechanical enhancement of an entangled sensor in a real environment, our achievements provide important information toward understanding the properties of an entangled sensor: (i) As the performance of the entangled sensor

strongly depends on the properties of the environment, systematic experimental analysis of the entangled sensor operating under various types of noise is essential for the realization of quantum-enhanced sensing, and therefore our experimental investigation with the NMR model provides insights to assess the practicality of quantum sensors. (ii) Our NMR method can be implemented with commonly available experimental apparatus (which almost every university owns) at room temperature, and therefore experimentalists can use this model as a testbed or a simulator before attempting to construct a real entangled sensor. For example, experimentalists can first use our NMR model to evaluate the pulse sequences that are expected to apply to the entangled sensor in a real environment.

The remainder of the paper is organized as follows. In Section II, we closely follow References [12, 13] and review how an entangled sensor is simulated using a star topology molecule. We then present a method demonstrating how to prepare a controlled environment following Ref. [19]. Note that an engineered noisy environment in Ref. [19] is equivalent to a controlled one in this paper. Finally, these two ideas are combined, and we simulate the entangled sensor in a controlled environment. We present experimental results in Section III, where the dynamics of the entangled sensor are evaluated in a time-inhomogeneous noisy environment, and a successful application of a dynamical decoupling technique [20] applied to the entangled sensor is demonstrated. Finally, Section IV presents a summary of our findings.

## II. THEORY

In this section, we describe our strategy to combine two ideas: (i) use of a star-topology molecule as an entangled magnetic sensor, and (ii) controlling the environment that surrounds the sensor.

### A. Molecules as a Simulator of an Entangled Magnetic Sensor

Assume an isolated nuclear spin with state

$$|+\rangle = \frac{|0\rangle + |1\rangle}{\sqrt{2}}, \quad (1)$$

where  $|0\rangle$  and  $|1\rangle$  are two eigenstates of the standard Pauli matrix  $\sigma_z$ . The system is exposed to a magnetic field  $B\vec{z}$ , where  $\vec{z}$  is the unit vector along the  $z$ -axis, for a period  $\tau$ , and becomes

$$|+\tau\rangle = \frac{|0\rangle + e^{i\gamma_G B \tau}|1\rangle}{\sqrt{2}}, \quad (2)$$

where  $\gamma_G$  is the gyromagnetic ratio. Therefore, the acquired phase  $\gamma_G B \tau$  can be used to measure  $B$ . The sensitivity of a set of  $N$  spins is proportional to  $\sqrt{N}$ , which is the SQL [5, 21].

Now, if we assume that our sensor consists of  $N$  spins and that the initial state is entangled, such that

$$|+\text{ent}\rangle = \frac{|00\dots 0\rangle + |11\dots 1\rangle}{\sqrt{2}}, \quad (3)$$

then, this state will evolve to

$$|+\text{ent},\tau\rangle = \frac{|00\dots 0\rangle + e^{iN\gamma_G B \tau}|11\dots 1\rangle}{\sqrt{2}}, \quad (4)$$

after time  $\tau$  elapses, and thus the sensitivity is proportional to the number of spins  $N$ , which is the Heisenberg Limit [5, 21].

Jones et al. demonstrated the above measurement scheme with star-topology molecules, as schematically shown in Fig. 1(a). They employed two molecules, trimethyl phosphite (TMP) [12] and tetramethylsilane (TMS) [13]. A TMP (or TMS) molecule consists of a center  $^{31}\text{P}$  ( $^{29}\text{Si}$ ) and three (four) methyl groups, and thus the center  $^{31}\text{P}$  ( $^{29}\text{Si}$ ) is surrounded by 9 (12)  $^1\text{H}$  spins. The highly symmetric structures of these molecules allow addressing of all surrounding spins (small open circles in Fig. 1(a)) globally, and thus the operations required to measure a magnetic field can be simplified.

In this work, we employed the simplest star topology molecule, which consists of a center spin ( $\circ$ ) and two side spins ( $\circ$ 's), as shown in Fig. 1(b).

We take the initial density matrix  $|0\rangle\langle 0| \otimes \frac{\sigma_0}{2} \otimes \frac{\sigma_0}{2}$  [22] (see also the Appendix). The state of the center spin is  $|0\rangle\langle 0|$ , while the two side spins are in a fully mixed state. When a magnetic field is applied only to the center spin ( $\circ$ ), i.e., the star-topology structure is not effective, the density matrix becomes

$$\rho_{\circ} = \frac{1}{8} \begin{pmatrix} 1 & e^{-i\theta} \\ e^{i\theta} & 1 \end{pmatrix} \otimes \sigma_0 \otimes \sigma_0, \quad (5)$$

after the magnetic field is applied. Here,  $\theta = \gamma_G B \tau$ , and the subscript  $\circ$  stands for the case when the center spin is exposed to the field. This case corresponds to non-entangled sensor.

Next, consider the case when the magnetic field is applied to the side spins ( $\circ$ 's), as shown in Fig. 1(d). This case corresponds to an entangled sensor. In a frame that co-rotates with

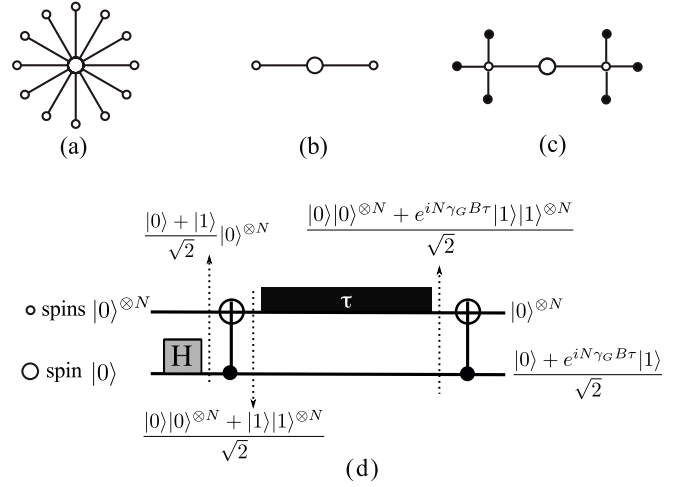


FIG. 1. (a, b, and c) Three different interaction topologies among spins ( $\circ$ ,  $\circ$ , and  $\bullet$ ) discussed in this study and (d) quantum circuit for an entangled magnetic field sensor simulation. (a) Sketch of a star-like interaction structure among spins, and (b) the simplest star topology structure. The small open circles ( $\circ$ 's) in (a) and (b) play the role of entangled sensors. (c) Two-step star topology structure used to conduct an entangled magnetic sensor simulation under a controlled environment. The large open circle ( $\circ$ ) is called the center spin, while the small open circles ( $\circ$ 's) are the side spins and play the role of an entangled sensor. The six surrounding solid circles ( $\bullet$ 's) are introduced in order to generate a time-inhomogeneous noisy environment acting on the entangled sensor. We refer to them as the environmental spins. (d) Basic quantum circuit used for measurements. Because of the symmetry of the interaction structure, all  $\circ$  spins can be accessed globally.

the center spin, it does not acquire a phase during the period  $\tau$ . The initial state  $\frac{1}{4}|0\rangle\langle 0| \otimes \sigma_0 \otimes \sigma_0$  can be decomposed to

$$\frac{1}{4}(|000\rangle\langle 000| + |011\rangle\langle 011| + |001\rangle\langle 001| + |010\rangle\langle 010|), \quad (6)$$

and thus, the final density matrix after the measurement operation is

$$\begin{aligned} \rho_{\circ} &= \frac{1}{8} \begin{pmatrix} 1 & 0 & 0 & 0 & e^{-2i\theta} & 0 & 0 & 0 \\ 0 & 1 & 0 & 0 & 0 & 1 & 0 & 0 \\ 0 & 0 & 1 & 0 & 0 & 0 & 1 & 0 \\ 0 & 0 & 0 & 1 & 0 & 0 & 0 & e^{2i\theta} \\ e^{2i\theta} & 0 & 0 & 0 & 1 & 0 & 0 & 0 \\ 0 & 1 & 0 & 0 & 0 & 1 & 0 & 0 \\ 0 & 0 & 1 & 0 & 0 & 0 & 1 & 0 \\ 0 & 0 & 0 & e^{-2i\theta} & 0 & 0 & 0 & 1 \end{pmatrix} \\ &= \frac{1}{8} \begin{pmatrix} 1 & e^{-2i\theta} \\ e^{2i\theta} & 1 \end{pmatrix} \otimes |00\rangle\langle 00| \\ &+ \frac{1}{8} \begin{pmatrix} 1 & e^{2i\theta} \\ e^{-i2\theta} & 1 \end{pmatrix} \otimes |11\rangle\langle 11| \\ &+ \frac{1}{8} \begin{pmatrix} 1 & 1 \\ 1 & 1 \end{pmatrix} \otimes (|01\rangle\langle 01| + |10\rangle\langle 10|), \quad (7) \end{aligned}$$

where  $\circ$  stands for the case when the magnetic field is applied to the side spins. Note that owing to the twice as large

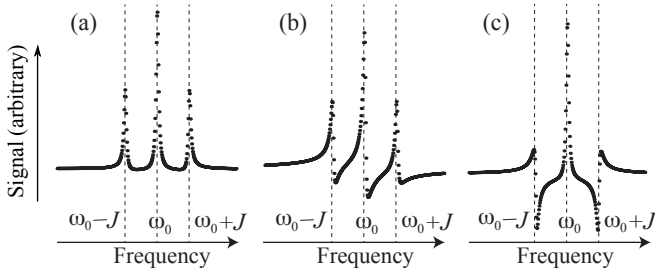


FIG. 2. Theoretical spectra calculated from  $S_k(t)$  for the case when  $JT_2 = 22$ . (a)  $\theta = 0^\circ$ , (b)  $\theta = 50^\circ$  for  $S_{\circ}(t)$ , (c)  $\theta = 50^\circ$  for  $S_{\circ}(t)$ . The frequency difference of these peaks is  $J$ , and the frequency of the center peaks is  $\omega_0$ .

phase accumulation ( $2\theta$ , instead of  $\theta$ ) of the initial states of  $|000\rangle\langle 000|$  and  $|011\rangle\langle 011|$ , the sensitivity of the side spins (the entangled sensor) interacting with the magnetic fields becomes twice as large as that of the center spin (non-entangled sensor).

Next, the method of how to detect the acquired phases in the NMR is presented. The state  $\rho_k$  ( $k = \circ, \bullet$ ) is assumed to develop under the Hamiltonian

$$H = \omega_0 \frac{\sigma_z}{2} \otimes \sigma_0 \otimes \sigma_0 + J \left( \frac{\sigma_z}{2} \otimes \frac{\sigma_z}{2} \otimes \sigma_0 + \frac{\sigma_z}{2} \otimes \sigma_0 \otimes \frac{\sigma_z}{2} \right), \quad (8)$$

where  $\omega_0$  corresponds to a Larmor frequency of the center spin and  $J$  is a coupling constant between the center spin and the two side spins.  $\omega_0$  is introduced to identify the signal originating from the center spin in the frequency domain signal. The signal from the center spin is [23–25]

$$S_k(t) = \text{Tr} \left( \left( (\sigma_x + i\sigma_y) \otimes \sigma_0 \otimes \sigma_0 \right) e^{-iHt} \rho_k e^{iHt} \right). \quad (9)$$

Therefore, the expected normalized signals are

$$S_{\circ}(t) = \frac{1}{4} e^{-t/T_2} \left( e^{-iJt} + 2 + e^{iJt} \right) \cos(\omega_0 t + \theta), \quad (10)$$

$$S_{\bullet}(t) = \frac{1}{4} e^{-t/T_2} \left( e^{-iJt - i2\theta} + 2 + e^{iJt + i2\theta} \right) \cos \omega_0 t, \quad (11)$$

where  $T_2$  is a phenomenological transverse relaxation time constant that is introduced for the signal to decrease exponentially. Equation (10) corresponds to the signal when the field is applied to the center spin (non-entangled sensor), while Eq. (11) corresponds to the case when the field is applied to the side spins (entangled sensor). Note the difference in the position of  $\theta$  in  $S_k(t)$ . The three terms in parentheses in  $S_k(t)$  correspond to three peaks that are observed when the  $S_k(t)$ 's are Fourier transformed (see Fig. 2).

### B. Controlled environment

Our idea to control the environment is demonstrated in Fig. 3. If System I directly interacts with a Markovian environment, it decays exponentially. If it interacts with a Markovian environment through System II, it exhibits various decay

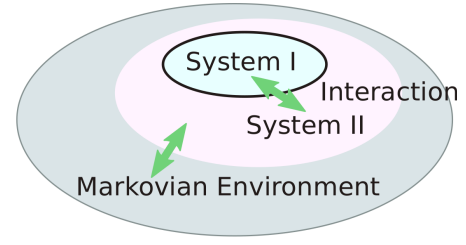


FIG. 3. (Color online) Controlled environment. Herein, the Markovian environment indirectly interacts with System I through System II.

behaviors, because System II acts as a memory of the controlled non-Markovian environment formed by System II and the Markovian environment [22, 26–30].

The chain of spins ( $\circ - \circ - \circ$  in Fig. 1(c)) is regarded as the sensor where the side spins (two  $\circ$ 's) accumulate the phase under the external field, and this phase is measured via the center spin ( $\circ$ ), as discussed in Sect. II A. The side spins ( $\circ$ 's) are surrounded by two sets of three spins (three  $\bullet$ 's), which we call environmental spins. We regard the side spins (the two  $\circ$ 's) as two independent System I's, while we consider the two sets of  $\bullet$ 's as two System II's. These environmental spins, with the Markovian environment outside them, act as a time-inhomogeneous noisy environment applied to the side spins (two  $\circ$ 's) as we previously discussed in Refs. [22, 26–30]. Note that only the nearest neighbor interactions are assumed important in this discussion. After all, we can control the environment of the sensor ( $\circ - \circ - \circ$ ).

## III. EXPERIMENTS

In this section, we describe our approach to simulate an entangled sensor in a controlled environment with a molecule solved in an isotropic liquid. First, we show how to prepare the Markovian controlled environment and then discuss how to simulate the entangled sensor in the controlled environment.

### A. Markovian controlled environment

Solute molecules in an isotropic liquid move rapidly and are influenced by a strong external magnetic field. Thus, the interactions among nuclear spins in the solute and solvent molecules are averaged out [31]. In other words, the solute molecules are approximated to be isolated systems.

To control a Markovian environment, magnetic impurities, such as Fe(III), are added to the solution. Because the added magnetic impurities move rapidly and randomly, they produce a Markovian environment, which flip-flops the solute molecules' nuclear spins randomly. The flip-flopping rate is proportional to the concentration of the magnetic impurities [26]. Moreover, we emphasize that the nuclear spins of

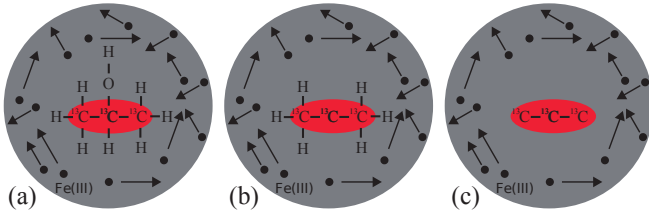


FIG. 4. (Color online) Sketch of a 2-propanol molecule in acetone-d6 with added magnetic impurities (Fe(III) ions). The chain of the  $^{13}\text{C}$  spins is surrounded by the H spins. These H spins can be selectively nullified by decoupling techniques, which provide three different controlled environments. The gray areas correspond to the System II's and Markovian environments. We consider three cases: (a) without decoupling, (b) selective decoupling of the H spin attached to the center  $^{13}\text{C}$ , and (c) full decoupling of all H spins.

System II are more strongly influenced by the magnetic impurities than the inner ones (System I) because the dipole-dipole interactions are short-range [19].

## B. Sample and controlled environment

The two-step star-topology molecule that we employ in this work is 2-propanol solved in acetone d6 with Fe(III) magnetic impurities added. The structure of this molecule is shown in Fig. 4(a). The three  $^{13}\text{C}$  spins correspond to  $\circ - \bigcirc - \circ$  in Fig. 1(b, c), while the H spins are employed as System II in Fig. 3. We can selectively nullify the H spins by dynamical decoupling techniques [20, 31], as shown in Fig. 4(a, b, c): (a) without decoupling, (b) selective decoupling of the H spin attached to the center  $^{13}\text{C}$  (hereafter, referred to as the selective-decoupling case), and (c) full decoupling of all H spins (hereafter, referred to as the full-decoupling case). This implies that the behavior of an entangled magnetic sensor in three different controlled environments can be studied. Note that the interaction topology of Fig. 1(c) can be realized in the case of Fig. 4(b). The obtained spectra shown in Fig. 5 exhibit clear differences according to the interaction topology differences presented in Fig. 4(a, b, c).

The Hamiltonian governing the nuclear spin dynamics of 2-propanol is given as

$$\mathcal{H} = \sum_j \omega_0^{(j)} \frac{\sigma_z^{(j)}}{2} + \sum_{j < k} J^{(j,k)} \frac{\sigma_z^{(j)} \otimes \sigma_z^{(k)}}{4}, \quad (12)$$

because  $|\omega_0^{(j)} - \omega_0^{(k)}| \gg J^{(j,k)}$ ;  $\omega_0^{(j)}$  is the isotropic chemically shifted Larmor frequency of the  $j$ 'th spin, and  $J^{(j,k)}$  represents the interaction strength between the  $j$ 'th and  $k$ 'th spins [27, 31].  $\omega_0^{(j)}$  and  $J^{(j,k)}$  were measured from the spectra of a sample without magnetic impurities and are summarized in Table I.

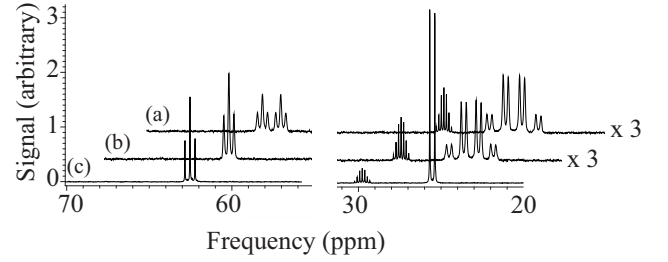


FIG. 5. Spectra of the  $^{13}\text{C}$  spins in different decoupling conditions: (a) without decoupling, (b) selective decoupling by applying a small continuous RF excitation, whose frequency is the Larmor frequency of HC (the H spin attached to CC), and (c) full decoupling by applying the WALTZ sequence to all H spins. The sample is 0.41 M  $^{13}\text{C}$ -labeled 2-propanol in acetone-d6 with 12 mM of Fe(III)acac. The peaks at 62.6 ppm are originated from the center  $^{13}\text{C}$  of the chain, while those at 25.5 ppm are originated from the side  $^{13}\text{C}$ 's. The spectra in (a) and (b) are magnified three times.

TABLE I.  $\omega_0^{(j)}$  and  $J^{(j,k)}$  are summarized. We label the spins as CC (the center  $^{13}\text{C}$  in the C spin chain), CSs (the two side  $^{13}\text{C}$ 's in the C spin chain), HC (the H spin attached to CC) and HSs (the H spins attached to a CS). Diagonal elements are the  $\omega_0^{(j)}$ 's in ppm, while the off-diagonal elements are those of  $J^{(j,k)}$  in rad/s. NR implies that these values are too low to be measured reliably.

$j \backslash k$	CC	CSs	HC	HSs
CC	62.6 ppm	$2\pi \cdot 38.4$ rad/s	$2\pi \cdot 140$ rad/s	$2\pi \cdot 4.4$ rad/s
CSs		25.5 ppm	NR	$2\pi \cdot 124$ rad/s
HC			3.78 ppm	NR
HSs				1.21 ppm

## C. Simulation of Entangled Sensor

We implemented the quantum circuit shown in Fig. 1(d) under standard NMR pulse sequences [25]. The rotation operations applied to CC are

$$R_C(\phi, \theta) = R(\phi, \theta) \otimes \sigma_0 \otimes \sigma_0, \quad (13)$$

$$Z_C(\theta) = Z(\theta) \otimes \sigma_0 \otimes \sigma_0, \quad (14)$$

where  $R(\phi, \theta) = e^{-i\theta(\sigma_x \cos \phi + \sigma_y \sin \phi)/2}$  and  $Z(\theta) = e^{-i\theta\sigma_z/2}$ .  $\theta$  in  $R(\theta, \phi)$  is the rotation angle and  $\phi$  defines the rotation axis in the  $xy$ -plane from the  $x$ -axis, while  $\theta$  in  $Z(\theta)$  is the rotation angle about the  $z$ -axis. The rotations that operate on the CSs can be implemented simultaneously because of the symmetry of the molecular structure and are defined as

$$R_S(\phi, \theta) = \sigma_0 \otimes R(\phi, \theta) \otimes R(\phi, \theta), \quad (15)$$

$$Z_S(\theta) = \sigma_0 \otimes Z(\theta) \otimes Z(\theta). \quad (16)$$

The Hadamard gate on CC was effectively implemented with an  $R_C(\pi/2, -\pi/2)$ , while a pseudo-CNOT gate was realized as

follows:

$$\begin{aligned} \text{CNOT} &= e^{-i\frac{\pi}{4}} Z_C(-\frac{\pi}{2}) Z_S(-\frac{\pi}{2}) R_C(0, \frac{\pi}{2}) U_E R_S(\frac{\pi}{2}, \frac{\pi}{2}) \\ &= \begin{pmatrix} 1 & 0 & 0 & 0 & 0 & 0 & 0 & 0 \\ 0 & 1 & 0 & 0 & 0 & 0 & 0 & 0 \\ 0 & 0 & 1 & 0 & 0 & 0 & 0 & 0 \\ 0 & 0 & 0 & 1 & 0 & 0 & 0 & 0 \\ 0 & 0 & 0 & 0 & 0 & 0 & 0 & i \\ 0 & 0 & 0 & 0 & 0 & 0 & i & 0 \\ 0 & 0 & 0 & 0 & 0 & i & 0 & 0 \\ 0 & 0 & 0 & 0 & i & 0 & 0 & 0 \end{pmatrix}, \end{aligned} \quad (17)$$

where  $U_E = e^{-\pi(\sigma_z \otimes \sigma_z \sigma_0 + \sigma_z \otimes \sigma_0 \sigma_z)/4}$ .  $U_E$  was implemented by waiting for a period of  $\frac{n}{\Delta\omega_0}$ , where  $\Delta\omega_0$  is the Larmor frequency difference between CC and CSs.  $n$  is an integer and is selected so that  $\frac{n}{\Delta\omega_0} \approx \frac{\pi}{J^{(\text{CC,CSs})}}$  (see Table I). All  $Z_k(\theta)$ 's ( $k = C$  or  $S$ ) were virtually implemented by controlling the  $\phi$ 's in the  $R_k(\phi, \theta)$ 's ( $k = C$  or  $S$ ) [32]. We employed jump-and-return pulses [33] to realize  $R_k(\phi, \theta)$  with concatenated composite pulses (reduced CInBB) [34, 35] to reduce any errors caused by imperfect pulses.

Magnetic field sensing is equivalent to measuring the phase difference between the initial and final state of CC, as shown in Fig. 1. Therefore, we simulated the magnetic field by applying a  $Z_k(\theta)$ -rotation,

#### field on CC:

$$\left( R_C(-\frac{\pi}{2}, \frac{\pi}{2}) - Z_C(\theta) \right) - \text{CNOT} - \left( \frac{\tau}{2} - R_S(0, \pi) - \frac{\tau}{2} \right) - \text{CNOT},$$

#### field on CSs:

$$R_C(-\frac{\pi}{2}, \frac{\pi}{2}) - (\text{CNOT} - Z_S(\theta)) - \left( \frac{\tau}{2} - R_S(0, \pi) - \frac{\tau}{2} \right) - \text{CNOT},$$

where  $(\tau/2 - R_S(0, \pi) - \tau/2)$  is the period when the entangled sensor acquires the phase  $\theta = \gamma_G B \tau$  in real measurements. In our simulations, the ‘‘entangled magnetic sensor’’ (CSs) is active in the controlled environment only during this period.  $R_S(0, \pi)$  in the middle of this period was added to nullify the time development caused by the interaction between CC and CSs. We started from the thermal state and observed only CC in our simulations.

We first demonstrate the ‘‘entanglement-enhanced’’ phase sensitivity [12, 36, 37] in the full-decoupling case (Fig. 4(c)). A sample consisting of 0.41 M  $^{13}\text{C}$ -labeled 2-propanol solved in acetone- $d_6$  with 12 mM of Fe(acac) as a magnetic impurity was used. The  $T_1$ 's of  $^{13}\text{C}$  of this sample were measured to be 1.3 s, while the  $T_1$ 's of all H spins were approximately 100 ms. Figure 6 shows the spectra of CC as a function of  $\theta$  (the ‘‘field strength’’) at  $\tau = 3.4$  ms. When the ‘‘field’’ was applied to CC (Fig. 6 (upper), the non-entangled sensor), the three peaks acquired the same amount of phase. These phases were the same as  $\theta$  given by  $Z_C(\theta)$  within an acceptable experimental error range. Note the good agreement between the measured and calculated spectra. On the other hand, the acquired phases were depending on peaks when the ‘‘field’’ was applied to CSs (Fig. 6 (lower), entangled sensor). The center peak does not acquire any phase, as one can see from the fact

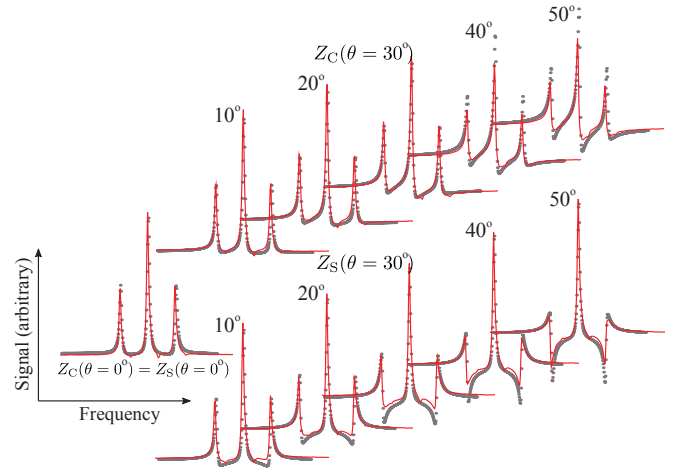


FIG. 6. (Color online) Spectra as functions of  $\theta$  (the strength of the ‘‘magnetic field’’) when all H spins were decoupled (full-decoupling case). The red solid lines are measured spectra, while the grey dots are the calculated theoretical spectra, such as in Fig. 2. The left-most spectra is the reference without a ‘‘magnetic field’’. The upper spectra show cases when ‘‘magnetic field’’s were applied to CC (non-entangled sensor), while the lower ones correspond to CSs (the entangled sensor). The frequencies of the center peaks are 62.6 ppm and the frequency differences among the peaks are  $2\pi \cdot 38.4$  rad/s, as listed in Table I.

that it is symmetric, regardless of the  $\theta$  values. The two side peaks acquire  $\pm 2\theta$ ; the + sign is for the left peak and the - sign is for the right. Again, we obtain reasonably good agreement between the measured and calculated spectra, although the measured spectra are not as sharp as the calculated spectra. The case of the non-entangled sensor appears to result in better agreement between the experiments and theory compared to that of the entangled sensor. We explain this result as follows. The phase (‘‘field’’) information is stored in the entangled spins (o’s) in the latter case and we therefore expect that this information is more fragile than that in the former case because of the fragility of the entangled state. All calculated spectra were obtained with the measured coupling constant of  $J^{(\text{CC,CSs})} = 2\pi \cdot 38.4$  rad/s and two fitting parameters: one being  $T_2 = 0.1$  s and the other being the amplitude. The value of  $T_2$  is quite reasonable based on the FID signal measurements. Therefore, the amplitude is the only fitting parameter required.

Next, we show that the ‘‘magnetic field sensing’’ was affected by ‘‘noise’’ generated by the controlled environment and that the ‘‘noise’’ can be suppressed by a dynamical decoupling technique (XY-8 [20]). Here, HS (corresponding to a  $\bullet$  in Fig. 1(c)) and magnetic impurities combine to generate a time-inhomogeneous noisy environment acting on the entangled sensor (that corresponds to the o’s in Fig. 1(c)). We can nullify the time-inhomogeneous noisy environment by effectively removing the HSs with a decoupling technique. The experimental details are as follows. We consider two cases: the full-decoupling case (Fig. 4(c)) and the selective-decoupling case (Fig. 4(b)). In the full-decoupling case, the magnetic impuri-



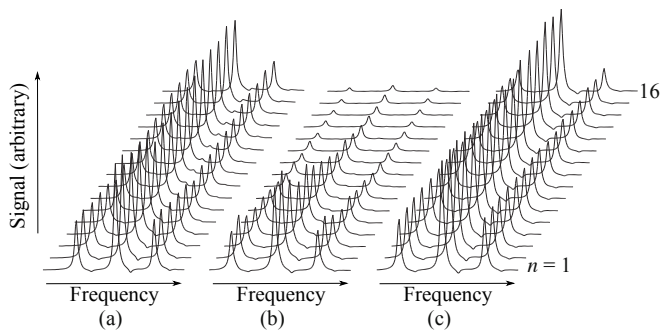


FIG. 7. Measurements in various noisy environments as a function of measurement time  $\tau (= 3.44 \text{ ms} \times n)$ . (a) “without noise” by decoupling all H spins (full-decoupling case), (b) “under noise” without decoupling HSs (selective-decoupling), and (c) “under noise,” where the noise is suppressed by a dynamical decoupling technique (XY-8) during measurements. The frequency of the center peaks is 62.6 ppm and the frequency differences among the peaks are  $2\pi \cdot 38.4 \text{ rad/s}$ , as listed in Table I.

ties produce weak effects on CC and CSs [19], and thus we can state that “magnetic field sensing” was performed under an approximately noiseless environment in the short time scale of less than 50 ms in the experiment. This approximation was confirmed by the fact that the signal exhibited little decay in this time scale (see Fig. 7(a)). In the selective decoupling case, CSs should be affected by the time-inhomogeneous noisy environment formed by the HSs and the magnetic impurities. This noisy environment was also confirmed by the fact that the signal decays quickly, as shown in Fig. 7(b). The relaxation constant is approximately 30 ms. The spectra in Fig. 7(c) were measured when the HSs were not decoupled (the same as (b)), but the XY-8 sequence was applied to CC and CSs simultaneously. The signals decay much more slowly than those in (b), which indicates that the dynamical decoupling was effective in protecting the entangled sensor. When a dynamical decoupling technique is applied to a sensor, it cannot detect the DC component, but can measure the AC one, whose frequency is determined by the decoupling technique [2]. Therefore, it is possible to construct an entanglement-enhanced AC magnetic field sensor under time-inhomogeneous noise, as theoretically predicted in Refs. [15–18].

#### IV. SUMMARY

We have successfully modeled an entangled magnetic field sensor in various noisy environments using NMR techniques. In our model, a sensor is a star-topology molecule, 2-propanol, solved in acetone-d<sub>6</sub>, and the magnetic field is simulated by rotational pulse sequences acting on the sensor. The environment surrounding a sensor can be controlled by adding Fe(III) as an impurity in the solvent and by selectively decoupling H spins in the 2-propanol molecule. We have demonstrated the entanglement-enhanced phase sensitivity and have discussed its enhancement mechanism. We further demonstrate that magnetic field sensing is affected by noise. Im-

portantly, we have demonstrated that when the noise is time-inhomogeneous, its effect can be suppressed by a dynamical decoupling technique during the entanglement-enhanced magnetic field sensing period.

#### ACKNOWLEDGMENTS

This work was supported by CREST(JPMJCR1774), JST. This work is also supported by Leading Initiative for Excellent Young Researchers MEXT Japan and MEXT KAKENHI (Grant No. 15H05870).

#### Appendix A

In previous work [19], we systematically studied the three cases when the environments consisted of 1, 3, and 12 spins + a Markovian environment generated by magnetic impurities. We add another case study here involving a 6 spins + Markovian environment case by using 2-propanol solved in acetone d<sub>6</sub>.

The longitudinal relaxation times,  $T_1$ ’s of the  $^{13}\text{C}$  spins of a 0.41 M  $^{13}\text{C}$ -labeled 2-propanol sample solved in acetone d-6 without magnetic impurities were measured to be 20 s (CC) and 8 s (CSs). Therefore, within a time scale much shorter than these  $T_1$ ’s, the  $^{13}\text{C}$  chain in the 2-propanol molecules can be approximated as isolated systems. We added magnetic impurities (Fe(III) acac) and prepared four samples, as listed in Table II.

TABLE II. Measured  $T_1$ ’s and  $T_2$ ’s of CC, and  $T_1$  of HSs are summarized.  $C_m$ : concentration of the magnetic impurity (Fe(III)acac),  $T_1$ : longitudinal relaxation time constant of CC,  $T_2^{(f)}$ : relaxation time constant of the signal in the full-decoupling case,  $T_2^{(s)}$ : relaxation time constant of the signal in the selective-decoupling case, and  $T_1(\text{HSs})$ : longitudinal relaxation time constant of HSs’ spins.

Sample	$C_m$ (mM)	$T_1$ (s)	$T_1 \cdot C_m$ (mM·s)	$T_2^{(f)}$ (ms)	$T_2^{(f)} \cdot C_m$ (M·s)	$T_2^{(s)}$ (ms)	$T_1(\text{HSs})$ (ms)
1	12	1.3	15	$3.0 \times 10^2$	$3.5 \times 10^{-3}$	$3.0 \times 10$	93
2	26	0.64	17	$1.0 \times 10^2$	$2.6 \times 10^{-3}$	$3.9 \times 10$	43
3	47	0.36	17	$9.9 \times 10$	$4.7 \times 10^{-3}$	$3.8 \times 10$	24
4	94	0.17	16	$6.4 \times 10$	$6.0 \times 10^{-3}$	$3.9 \times 10$	17

In the full-decoupling case, a small but not negligible direct influence of the Markovian environment on CC should be observed. The  $T_1$ ’s of CC in Table II are inversely proportional to the magnetic impurity concentration  $C_m$ , which implies that in this case,  $T_1$  is determined by the impurity concentration [26]. On the other hand, in the selective-decoupling case, the interaction between CC and the Markovian environment through the HSs (System II) should be added, although it is expected to be small. Therefore, we obtain the controlled environment, which consists of 6 spins + Markovian environment, which causes a non-exponential decay of CC [19]. We

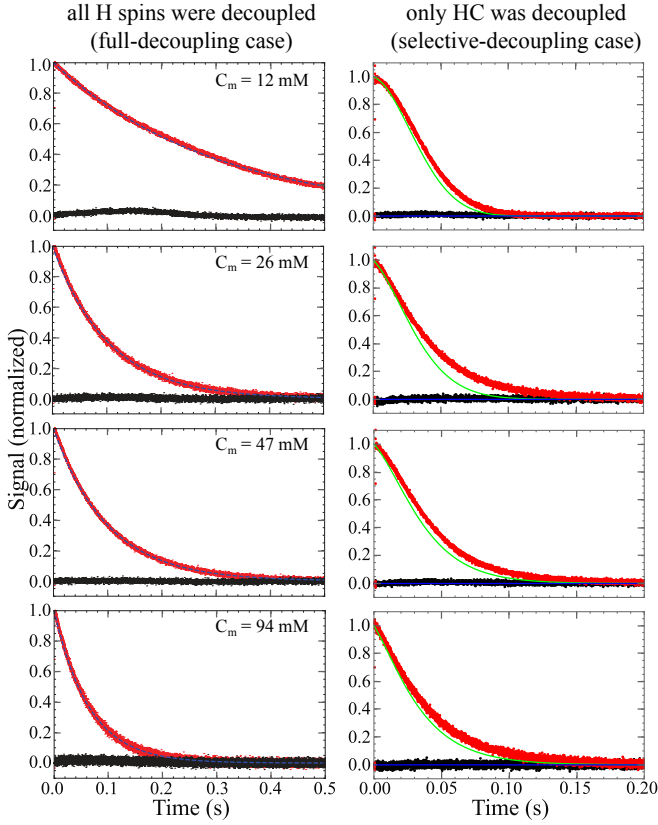


FIG. 8. (Color online) FID signals of Samples 1, 2, 3, and 4 in Table II. The initial states were  $|+\rangle\langle+| \otimes (|01\rangle\langle 01| + |10\rangle\langle 10|)$ . The real parts of the FID signals are shown in red, while the imaginary are shown in black. The full-decoupling cases are shown in the left panels and selective decoupling cases are presented in the right panels. The black dashed curves in the left panels are exponential fittings to the real parts of the FID signals. The green (blue) curves in the right panels are the calculated real (imaginary) parts of the FID signals [19]. The blue curves overlap the experimental data and thus are hardly visible.

note, however, that the large interactions between CC and CSs ( $J^{(CC,CSs)} = 2\pi \cdot 34$  rad/s) compared with those between CC and the HSs ( $J^{(CC,HSs)} = 2\pi \cdot 4.4$  rad/s) prevent direct observation of the subtle non-exponential dynamics.

To successfully observe the above subtle non-exponential dynamics, let us re-examine the thermal state  $\rho_{th}$  of the three

$^{13}\text{C}$ 's, which is [23–25]

$$\begin{aligned} \rho_{th} \approx & \underbrace{\frac{\sigma_0 + \epsilon|0\rangle\langle 0|}{2}}_{\text{CC}} \otimes \underbrace{\frac{\sigma_0}{2} \otimes \frac{\sigma_0}{2}}_{\text{CSs}} \\ & + \underbrace{\frac{\sigma_0}{2}}_{\text{CC}} \otimes \underbrace{\frac{\sigma_0 + \epsilon|0\rangle\langle 0|}{2}}_{\text{CSs}} \otimes \frac{\sigma_0}{2} \\ & + \underbrace{\frac{\sigma_0}{2}}_{\text{CC}} \otimes \underbrace{\frac{\sigma_0}{2} \otimes \frac{\sigma_0 + \epsilon|0\rangle\langle 0|}{2}}_{\text{CSs}} \end{aligned} \quad (\text{A1})$$

Here,  $\epsilon \sim 10^{-5}$  in NMR measurements. When we observe only CC,  $\rho_{th}$  is equivalent to

$$\rho_{th} \approx \frac{1}{8} (\sigma_0 + \epsilon|0\rangle\langle 0|) \otimes (|0\rangle\langle 0| + |1\rangle\langle 1|) \otimes (|0\rangle\langle 0| + |1\rangle\langle 1|).$$

Moreover,  $\sigma_0$  of CC is not observable in NMR and thus  $\rho_{th}$  can be re-normalized as

$$\rho_{th} \approx \frac{1}{8} (|0\rangle\langle 0|) \otimes (|00\rangle\langle 00| + |01\rangle\langle 01| + |10\rangle\langle 10| + |11\rangle\langle 11|).$$

The interaction effects on CC from the  $|01\rangle\langle 01|$  and  $|10\rangle\langle 10|$  states of CSs cancel each other out. Thus if we can prepare

$$\rho_i = |+\rangle\langle+| \otimes (|01\rangle\langle 01| + |10\rangle\langle 10|), \quad (\text{A2})$$

we can observe the subtle non-exponential dynamics discussed previously. This  $\rho_i$  can be prepared with a standard NMR technique called a soft pulse [31].

The results are summarized in Fig. 8. We can successfully observe the exponential decays in the full decoupling cases (left panels), while the non-exponential decay dynamics are observed in the selective decoupling cases (right panels). We also calculated the decay dynamics from the data (summarized in Table II) as in our previous work [19], which are plotted as green (blue) solid curves in the right panels in Fig. 8. By taking into account that there are no fitting parameters except for the amplitude, we believe that the calculated dynamics reproduce the observations relatively well. However, the reproducibility may not be as good as in our preceding work [19], which may be caused by the imperfect soft pulses employed for preparing the initial state or by the error in parameter determination summarized in Table II, especially regarding the interaction strength between CC and the HSs ( $J^{(CC,HSs)}$ ).

- 
- [1] M. Nielsen and I. Chuang, *Quantum Computation and Quantum Information*, Cambridge Series on Information and the Natural Sciences (Cambridge University Press, 2000).  
 [2] C. L. Degen, F. Reinhard, and P. Cappellaro, *Rev. Mod. Phys.* **89**, 035002 (2017).  
 [3] T. Fernholz, H. Krauter, K. Jensen, J. F. Sherson, A. S. Sørensen, and E. S. Polzik, *Phys. Rev. Lett.* **101**, 073601 (2008).  
 [4] W. Wasilewski, K. Jensen, H. Krauter, J. J. Renema, M. V. Bal-

- abas, and E. S. Polzik, *Phys. Rev. Lett.* **104**, 133601 (2010).  
 [5] V. Giovannetti, S. Lloyd, and L. Maccone, *Nature Photonics* **5**, 222 EP (2011).  
 [6] D. Leibfried, B. DeMarco, V. Meyer, D. Lucas, M. Barrett, J. Britton, W. M. Itano, B. Jelenković, C. Langer, T. Rosenband, and D. J. Wineland, *Nature* **422**, 412 EP (2003).  
 [7] D. Leibfried, M. D. Barrett, T. Schaez, J. Britton, J. Chiaverini, W. M. Itano, J. D. Jost, C. Langer, and D. J. Wineland, *Science* **304**, 1476 (2004).

- <http://science.sciencemag.org/content/304/5676/1476.full.pdf>.
- [8] D. Leibfried, E. Knill, S. Seidelin, J. Britton, R. B. Blakestad, J. Chiaverini, D. B. Hume, W. M. Itano, J. D. Jost, C. Langer, R. Ozeri, R. Reichle, and D. J. Wineland, *Nature* **438**, 639 EP (2005).
- [9] V. Meyer, M. A. Rowe, D. Kielpinski, C. A. Sackett, W. M. Itano, C. Monroe, and D. J. Wineland, *Phys. Rev. Lett.* **86**, 5870 (2001).
- [10] C. Orzel, A. K. Tuchman, M. L. Fenselau, M. Yasuda, and M. A. Kasevich, *Science* **291**, 2386 (2001), <http://science.sciencemag.org/content/291/5512/2386.full.pdf>.
- [11] J. Appel, P. J. Windpassinger, D. Oblak, U. B. Hoff, N. Kjærgaard, and E. S. Polzik, *Proceedings of the National Academy of Sciences* **106**, 10960 (2009), <http://www.pnas.org/content/106/27/10960.full.pdf>.
- [12] J. A. Jones, S. D. Karlen, J. Fitzsimons, A. Ardavan, S. C. Benjamin, G. A. D. Briggs, and J. J. L. Morton, *Science* **324**, 1166 (2009), <http://science.sciencemag.org/content/324/5931/1166.full.pdf>.
- [13] S. Simmons, J. A. Jones, S. D. Karlen, A. Ardavan, and J. J. L. Morton, *Phys. Rev. A* **82**, 022330 (2010).
- [14] S. F. Huelga, C. Macchiavello, T. Pellizzari, A. K. Ekert, M. B. Plenio, and J. I. Cirac, *Phys. Rev. Lett.* **79**, 3865 (1997).
- [15] Y. Matsuzaki, S. C. Benjamin, and J. Fitzsimons, *Phys. Rev. A* **84**, 012103 (2011).
- [16] A. W. Chin, S. F. Huelga, and M. B. Plenio, *Phys. Rev. Lett.* **109**, 233601 (2012).
- [17] T. Tanaka, P. Knott, Y. Matsuzaki, S. Dooley, H. Yamaguchi, W. J. Munro, and S. Saito, *Phys. Rev. Lett.* **115**, 170801 (2015).
- [18] H.-P. Breuer, E.-M. Laine, J. Piilo, and B. Vacchini, *Rev. Mod. Phys.* **88**, 021002 (2016).
- [19] L. B. Ho, Y. Matsuzaki, M. Matsuzaki, and Y. Kondo, *New Journal of Physics* **21**, 093008 (2019).
- [20] D. Suter and G. A. Álvarez, *Rev. Mod. Phys.* **88**, 041001 (2016).
- [21] S. F. Huelga, C. Macchiavello, T. Pellizzari, A. K. Ekert, M. B. Plenio, and J. I. Cirac, *Phys. Rev. Lett.* **79**, 3865 (1997).
- [22] Y. Kondo, Y. Matsuzaki, K. Matsushima, and J. G. Filgueiras, *New Journal of Physics* **18**, 013033 (2016).
- [23] D. G. Cory, A. F. Fahmy, and T. F. Havel, *Proceedings of the National Academy of Sciences* **94**, 1634 (1997), <http://www.pnas.org/content/94/5/1634.full.pdf>.
- [24] N. A. Gershenfeld and I. L. Chuang, *Science* **275**, 350 (1997), <http://science.sciencemag.org/content/275/5298/350.full.pdf>.
- [25] Y. Kondo, “Liquid-state nmr quantum computer: Working principle and some examples, molecular realizations of quantum computing 2007 (kinki university series on quantum computing vol. 2) edited by m. nakahara, y. ota, r. rahimi, y. kondo, and m. tada-umezaki (singapore),” (World Scientific, 2009) pp. 1–52.
- [26] A. Iwakura, Y. Matsuzaki, and Y. Kondo, *Phys. Rev. A* **96**, 032303 (2017).
- [27] Y. Kondo and M. Matsuzaki, *Modern Physics Letters B* **32**, 1830002 (2018).
- [28] Y. Kondo, M. Nakahara, S. Tanimura, S. Kitajima, C. Uchiyama, and F. Shibata, *Journal of the Physical Society of Japan* **76**, 074002 (2007), <https://doi.org/10.1143/JPSJ.76.074002>.
- [29] B. M. Garraway, *Phys. Rev. A* **55**, 2290 (1997).
- [30] D. Tamascelli, A. Smirne, S. F. Huelga, and M. B. Plenio, *Phys. Rev. Lett.* **120**, 030402 (2018).
- [31] M. Levitt, *Spin Dynamics: Basics of Nuclear Magnetic Resonance* (Wiley, 2008).
- [32] Y. Kondo, M. Nakahara, and S. Tanimura, in *Physical Realizations of Quantum Computing: Are the DiVincenzo Criteria Fulfilled in 2004?*, edited by M. Nakahara, S. Kanemitsu, M. M. Salomaa, and S. Takagi, Kindai University (World Scientific, Osaka, Japan, 2006) p. 127.
- [33] M. D. Bowdrey and J. A. Jones, *Phys. Rev. A* **74**, 052324 (2006).
- [34] M. Bando, T. Ichikawa, Y. Kondo, and M. Nakahara, *Journal of the Physical Society of Japan* **82**, 014004 (2013), <https://doi.org/10.7566/JPSJ.82.014004>.
- [35] M. Bando, T. Ichikawa, Y. Kondo, N. Nemoto, M. Nakahara, and Y. Shikano, *Scientific Reports* **10**, 2126 (2020).
- [36] G.-Q. Liu, Y.-R. Zhang, Y.-C. Chang, J.-D. Yue, H. Fan, and X.-Y. Pan, *Nature Communications* **6**, 6726 EP (2015).
- [37] P. A. Knott, W. J. Munro, and J. A. Dunningham, *Nature Communications* **7**, 11520 EP (2016).